

Iron snow zones as a mechanism for generating Mercury's weak observed magnetic field

R. Vilim,¹ S. Stanley,¹ and S. A. Hauck II²

Received 20 October 2009; revised 16 July 2010; accepted 2 August 2010; published 12 November 2010.

[1] The anomalously weak observed magnetic field of Mercury is difficult to explain by appealing to crustal remanent magnetism or Earth-like dynamo mechanisms. Although the field is likely caused by a hydromagnetic dynamo, the field strength is far weaker than the characteristic strength expected from an active, strong field dynamo. Recent experimental work has shown that sources of compositional convection exist in mixtures of sulfur and iron at temperatures and pressures relevant to Mercury's core. The number and location of these iron "snow" zones is dependent on the sulfur content of the liquid portion of the core. We use a numerical dynamo model to show that the core states which include a snow zone midway through the core produce the observed field strength and expected field partitioning of the Mercurian magnetic field.

Citation: Vilim, R., S. Stanley, and S. A. Hauck II (2010), Iron snow zones as a mechanism for generating Mercury's weak observed magnetic field, *J. Geophys. Res.*, 115, E11003, doi:10.1029/2009JE003528.

1. Introduction

[2] Measurements from the Mariner 10 and more recent MESSENGER flybys of Mercury have revealed the presence of an internally generated magnetic field [Ness *et al.*, 1976; Anderson *et al.*, 2009], likely due to an active dynamo operating in the core of the planet. The most recent estimates from MESSENGER data place the dipole moment of this field between 180 and 220 nT- R_M^3 (where $R_M = 2440$ km, the mean radius of Mercury) tilted less than 5 degrees from the rotation axis [Anderson *et al.*, 2009; Uno *et al.*, 2009]. While the spatial and temporal extent of the current data does not allow resolution of higher multipoles, any dynamo generated field should possess them.

[3] The strength and structure of the Mercurian field is difficult to explain using the mechanisms which are thought to be responsible for the magnetic fields of other planets in the solar system. One possible explanation is that the field is due to remanent magnetization from a once active dynamo in the planet, as is the case on Mars. The large scale of the Mercurian magnetic field casts doubt on this hypothesis, since on the Earth and on Mars the crustal fields are much smaller scale. If crustal remanent magnetization is responsible, then the circumstances through which it formed must be unique to Mercury, since there is currently no evidence of small-scale crustal magnetization on Mercury [Purucker *et al.*, 2009]. Furthermore, Runcorn's theorem states that a homogenous spherical shell cannot be internally magnetized

to a dipolar field. Although the existence of crustal inhomogeneities relaxes the constraints set by Runcorn's theorem [Aharonson *et al.*, 2004], the observed field is likely too strong to be reasonably explained through crustal magnetization unless the magnetic mineral is both highly magnetized and very shallow.

[4] The most likely mechanism to explain Mercury's magnetic field is through an active dynamo operating within the core of the planet. However, the strength of the observed field is at odds with standard estimates for dynamo generated fields (established from studies of the Earth's field), therefore, Mercury's dynamo must be unique in the solar system.

1.1. Dynamo Explanations for Mercury's Field

[5] One way a dynamo could produce a weak surface field is through a non Earth-like field partitioning. There are several methods through which the magnetic field strength of Mercury can be estimated. One method assumes that to first order, the Coriolis and Lorentz forces will balance in the core; this is known as magnetostrophic balance. Magnetostrophic balance implies an estimated magnetic field strength of $B = \sqrt{2\Omega\rho Re_M/\sigma}$ where Ω is the rotation rate of the planet, ρ is the density, Re_M is the magnetic Reynolds number ($Re_M = UL/\eta$ where U and L are typical velocity and length scales, and η is the magnetic diffusivity), and σ is the electrical conductivity. If reasonable values are used for this estimate (Table 1), then a magnetic field strength within the core of $10^5 - 10^7$ nT is obtained.

[6] This estimation alone does not necessarily conflict with the observations of Mercury's field, since it predicts the magnetic field within the core while observations are made by spacecraft in the potential region outside the planet. The total magnetic field can be decomposed into

¹Department of Physics, University of Toronto, Toronto, Ontario, Canada.

²Department of Geological Sciences, Case Western Reserve University, Cleveland, Ohio, USA.

Table 1. Parameter Values and Field Strength Results^a

Model	Ra	Ra/Ra _C	Model Type	Dipole Moment (nT - R_M^3)			$B_{dip}/B_T \times 10^{-3}$			Normalized Power (deg)	
				Mean	Max	Min	Mean	Max	Min	P_2/P_1	P_3/P_1
1	50000	71	Double Snow State	190	304	82	4.06	30.3	0.42	0.069	0.37
2	50000	71	Double Snow State	394	676	151	2.50	10.9	0.44	0.091	0.24
3	55000	79	Double Snow State	166	246	64	2.07	8.2	0.61	0.097	0.15
4	65000	93	Double Snow State	875	1219	530	2.34	10.8	1.09	0.013	0.13
5	30000	43	Deep Snow State	1520	1617	1403	9.02	12.7	4.56	0.0012	0.011
6	55000	79	Deep Snow State	1028	1556	724	4.64	11.7	1.55	0.0096	0.085

^aRuns that have the same Rayleigh number have different initial conditions. We did this to ensure that the observed “double dynamo” state is robust. P_L refers to the power in the L th degree of the spherical harmonic power spectrum at the surface. The redimensionalization and field strength estimates use $\Omega = 1.24 \times 10^{-6} \text{ s}^{-1}$, $\rho = 7200 \text{ kg/m}^3$ (which is the same as is used by *Hauck et al.* [2004]), $\mu_0 = 4\pi \times 10^{-7} \text{ mkgs}^2 \text{ A}^2$, $U \approx 10^{-3} \text{ m/s}$, $L \approx 1800 \text{ km}$, and $\eta = 2 \text{ m}^2/\text{s}$. Of these, the length scale and the velocity estimation are the least certain.

poloidal \mathbf{B}_P and toroidal \mathbf{B}_T field components with the Helmholtz decomposition:

$$\mathbf{B} = \mathbf{B}_T + \mathbf{B}_P = \nabla \times (T\hat{\mathbf{r}}) + \nabla \times (\nabla \times (P\hat{\mathbf{r}})) \quad (1)$$

where T and P are the toroidal and poloidal scalars, and $\hat{\mathbf{r}}$ is the unit vector in the radial direction. Only the poloidal field has a radial component, and is therefore the only component that is observable from outside the core. If the Mercurian dynamo is similar to the Earth's in character, then there should be a similar partitioning between toroidal and poloidal field components. If the dipole moment at the core mantle boundary (CMB) is taken to be representative of the poloidal component, then it can be shown that for Mercury, $B_{dip} / B_T \approx 10^{-2} - 10^{-4}$, whereas for Earth $B_{dip} / B_T \approx 10^{-1}$ [*Stevenson*, 1987]. The conclusion from this analysis is that if Mercury exists in the strong field regime, then a distinctly non Earth-like field partitioning should be expected. Although this analysis is rather simplistic, it can be repeated using thermodynamic arguments instead of force balance arguments [*Schubert et al.*, 1988; *Stevenson*, 1987] resulting in similar total field strengths.

[7] Several studies [*Stanley et al.*, 2005; *Heimpel et al.*, 2005; *Christensen*, 2006; *Takahashi and Matsushima*, 2006] have produced dynamo models with dipole moments of the same order as the observed Mercurian field through anomalous field partitioning. This is accomplished either by making the inner core boundary (ICB) to core mantle boundary (CMB) radii ratios (r_{ic}) very small (0.15 in *Heimpel et al.* [2005]) or very large (0.8 in *Stanley et al.* [2005]).

[8] Another possibility is that Mercury's dynamo is not dipole dominated. Different scalings by *Olson and Christensen* [2006] have found that the dynamo should be in a state which produces a strong, multipolar dynamo. *Christensen* [2006] used evidence that the temperature gradient across the core mantle boundary may be sub-adiabatic to justify a stably stratified layer occupying the top portion of Mercury's core. He argues from local Rossby number considerations that Mercury's dynamo should be multipolar, and that the surrounding stable shell preferentially attenuates higher multipoles, leaving a slowly varying, weak dipolar field.

[9] The final way that a weak surface field has been produced involves appealing to interactions with the solar wind. *Glassmeier et al.* [2007] showed that Chapman-Ferraro currents induced by the interaction of Mercury's magnetosphere with the solar wind could produce magnetic fields in

its core which weaken the dynamo. Using a kinematic model based on work by *Levy* [1979], they showed that this “feedback dynamo” could account for the weak observed magnetic field of Mercury. The initial temporal evolution of this model was further investigated by *Heyner et al.* [2010].

1.2. State of Mercury's Core

[10] All dynamo explanations require that the core of Mercury remain at least partially liquid to the present day, something that is quite difficult to do with a small planet composed purely of iron. The detection of a dipolar magnetic field by Mariner 10 implied the existence of a liquid region due to the dynamo hypothesis, and recently published observational evidence of longitudinal librations [*Margot et al.*, 2007] strongly suggests the existence of a liquid layer in Mercury.

[11] Although there is likely a liquid region in Mercury's core, the size of the liquid outer core is not well constrained. Most studies attribute the existence of a liquid outer core to the presence of a light element, such as sulfur, which would depress the freezing point of iron. Like the size of the inner core, the sulfur content of the outer core is not well constrained. Thermal evolution models [*Schubert et al.*, 1988] have shown that while it is difficult to prevent the core of a planet as small as Mercury from freezing, if the core contains some sulfur it is possible to keep the core partially liquid to the present day. If other effects such as temperature- and pressure-dependent rheologies [*Conzelmann et al.*, 1999; *Hauck et al.*, 2004; *Breuer et al.*, 2007] or tidal dissipation [*Schubert et al.*, 1988] are accounted for, almost any inner core to outer core radius ratio can be produced. As a result, the size of the inner core remains rather unconstrained.

[12] Recent work by *Chen et al.* [2008] has shown through a combination of new experiments on the nonideal behavior of iron sulfur alloys at moderate pressures and existing data for higher-pressure melting of these alloys [*Stewart et al.*, 2007], that Mercury may have a very different core crystallization regime than any other body, save possibly Ganymede [*Hauck et al.*, 2006]. The result is the formation of an iron precipitate at different radii throughout the core, the exact location and number of which is dependent on sulfur content. Once an iron precipitate forms, it begins to sink, while the residual, more sulfur-rich liquid rises. The generation of iron “snow” acts as a source of compositional convection, affecting fluid motions and therefore the dynamo.

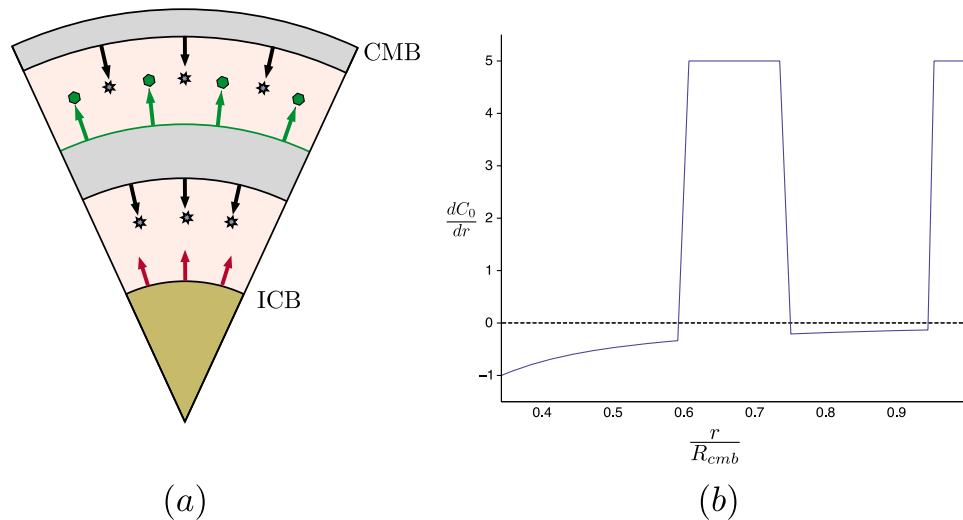


Figure 1. (a) A schematic diagram of a core in a double snow state; the snow layers are indicated by the gray bands. The compositional effects are indicated by arrows, sulfur driven effects are indicated in green (hexagons), while iron driven effects are in black (stars) and thermally driven effects are indicated by red arrows. (b) The slope of the background codensity profile for a double snow state. Areas of positive dC_0/dr indicate stably stratified regions, or snow zones. The dashed line indicates the neutral buoyancy profile ($dC_0/dr = 0$).

[13] If the liquid portion of the core contains between approximately 7 wt% and 8 wt% sulfur, an iron precipitate forms near the CMB and falls toward the inner core, this is referred to as a shallow snow state. For states with between approximately 8wt% and 10 wt% sulfur, a snow layer at approximately 23 GPa and deeper will form as well (a double snow state). In this case we would expect two sources of compositional convection, one from the dense iron precipitate falling toward the planetary center, and another from the liberated sulfur floating toward the CMB. A schematic of the “double snow state” scenario is shown in Figure 1a. Finally, if the liquid outer core contains more than 10 wt% sulfur, the snow zone at the CMB disappears, and only the deeper snow zone remains (a deep snow state). Although other light elements (such as O, Si, C, N, or H) can depress the freezing point of liquid iron, and could be present in Mercury’s core, the iron-sulfur system is the best characterized. At this point there is no evidence to suggest snow zones occur in systems with different constituents.

[14] Here we use a numerical dynamo model to examine whether the effects of snow zones on Mercury’s dynamo could explain its weak magnetic field. In the following sections we discuss a method of incorporating snow zones into the models, and the characteristics of the resulting fields. In this study we focus on double and deep snow states, since previous work demonstrated that shallow snow state models produce Earth-like dipole intensities when in magnetostrophic balance [Stanley and Mohammadi, 2008].

[15] We also exclude double and deep snow states in which the deep snow zone extends all the way to the ICB. In this scenario, motions in the lower region of the dynamo would be very small scale, since this region would be in a diffusive staircase convection regime. A state similar to this has already been explored by Stanley and Bloxham [2006] in the context of Uranus and Neptune. They found that

strong, multipolar fields result, which do not match the observed field of Mercury.

2. Numerical Model

[16] Numerical dynamo models operating in the strong field regime have reproduced many observations of planetary magnetic fields. Although at present they are unable to operate in the correct parameter regime, they have been instrumental in furthering our understanding of dynamo processes within planets. In addition, scaling arguments [Christensen and Aubert, 2006; Olson and Christensen, 2006] imply that in spite of the inability of modern dynamo models to operate in the correct parameter regime, dynamo models may be approaching an accurate scaling regime. Numerical dynamo models can be used to shed light on the dynamics of planetary cores by affording us an observable directly influenced by core dynamics: a magnetic field. For a discussion of the successes and shortcomings of geodynamo models, see Glatzmaier [2002] and Christensen and Wicht [2007].

[17] In this study we use the Kuang-Bloxham numerical dynamo model [Kuang and Bloxham, 1997, 1999], a 3D, nonlinear, Boussinesq dynamo model operating in a rotating spherical shell geometry. In this model the effects of temperature and composition have been combined into a single variable known as codensity. As they are both important effects in the core, ideally the dynamics of composition and temperature should be solved separately. Each have characteristic diffusivities, which differ by 3 orders of magnitude [Braginsky and Roberts, 1995], the thermal diffusivity being greater than the compositional diffusivity. In this study we adopt the common practice of assuming that small-scale (and unresolved) turbulence is present, this acts on both quantities equally and results in an effective turbulent dif-

fusivity which is the same for all quantities. This allows us to introduce a quantity known as the codensity C , which is a mixture of compositional and thermal differences with a common (large) diffusivity due to unresolved turbulence [Braginsky and Roberts, 1995; Wicht *et al.*, 2007].

[18] The model itself is fully nondimensional, the radius of the core r_o has been used as a length scale, $\tau = r_o^2 / \eta$ has been used as a time scale, and the magnetic field has been scaled according to $B = \sqrt{2\Omega\rho/\sigma}$. The codensity has been scaled according to $h_c r_o$ where h_c is the codensity flux at the inner core boundary. The nondimensional equations are

$$R_o \left(\frac{\partial}{\partial t} + \mathbf{u} \cdot \nabla \right) \mathbf{u} + \hat{\mathbf{z}} \times \mathbf{u} = -\nabla p + \mathbf{J} \times \mathbf{B} + Ra\Theta\mathbf{r} + E\nabla^2 \mathbf{u} \quad (2)$$

$$\frac{\partial C}{\partial t} + \mathbf{u} \cdot \nabla C = q_\kappa \nabla^2 C + Q \quad (3)$$

$$\frac{\partial \mathbf{B}}{\partial t} = \nabla \times (\mathbf{u} \times \mathbf{B}) + \nabla^2 \mathbf{B} \quad (4)$$

$$\nabla \cdot \mathbf{u} = 0 \quad (5)$$

Here \mathbf{B} , \mathbf{u} , and \mathbf{J} are the magnetic field, velocity, and current density, respectively, p is the modified pressure, $\hat{\mathbf{z}}$ is the rotation axis of the system, and C is the codensity.

[19] In the codensity transport equation (equation (3)), we implement codensity $C(\mathbf{r}, t)$ as a time-independent, stationary component ($C_0(r)$) plus a perturbation ($\Theta(\mathbf{r}, t)$):

$$C(\mathbf{r}, t) = C_0(r) + \Theta(\mathbf{r}, t) \quad (6)$$

Substituting into the codensity transport equation we find $C_0(r)$ by solving

$$\nabla^2 C_0(r) = -Q/q_\kappa \quad (7)$$

as it does not depend on time, while Θ solves

$$(\partial_t - q_\kappa \nabla^2) \Theta(\mathbf{r}, t) = -\mathbf{u} \cdot \nabla [\Theta(\mathbf{r}, t) + C_0(r)] \quad (8)$$

to capture the dynamical evolution of $C(\mathbf{r}, t)$. In the stationary codensity equation (equation (7)), Q can correspond to a source/sink term. For example, if convection is thermally driven, a constant Q can represent a volumetric radiogenic heating source. For compositionally driven convection, a constant Q can represent an evolution of the background density profile due to the release of light element. Here we will use a radially varying $Q(r)$ to implement snow zones.

[20] There are two effects which need to be taken into account when implementing a snow zone. First, the negative buoyancy representing the sinking iron, and secondly the positive buoyancy due to the remaining sulfur rich fluid. To incorporate both effects, we model a single snow zone as two thin shells: a source of codensity directly above a sink of codensity. The background codensity profile $C_0(r)$ is then determined by solving equation (7) with the given $Q(r)$. We find that a snow layer can be represented as a stably stratified layer in the slope of the background codensity profile. For the sake of simplicity, we make it a layer of constant $dC_0(r)/dr$ (Figure 1b). It should be noted that this representation of a snow layer does not

attempt to capture the specific dynamics of iron snow, but rather their net effects. Our model of a snow layer is quite crude, it will be the goal of future studies to make it more realistic.

[21] Our representation of a snow layer as a stably stratified region makes physical sense if we consider the path of an individual parcel buoyant at the ICB. This parcel will begin to rise, and will remain buoyant and rise until it reaches the base of the deep snow layer where it begins to solidify, expelling any light element mixed in with it, and losing its buoyancy. It then descends back into the lower layer. In this regard, the base of the snow layer is both a stably stratified layer (reducing the buoyancy of the rising parcel) and a source of compositional buoyancy in the lower layer (releasing iron which is denser than its surroundings). Similarly, the sulfur released in the deep snow layer is more buoyant than the fluid immediately above the deep snow layer and acts as a source of buoyancy for the upper region. For simplicity we do not consider the energy associated with latent heat release and consumption. Since compositionally driven convection is thermodynamically more efficient than the thermal component of convection, this is likely a reasonable first-order assumption.

[22] As a result of the large uncertainties associated with many of the quantities in planetary cores, the strength of the stable stratification due to the snow layer is unknown. In our models, we assume that the compositional sources of buoyancy resulting from iron snow zones are the primary driver of convection within Mercury, thus the stably stratified layer would be strongly stratified relative to the codensity flux at the inner core boundary. We found that our results remained largely the same so long as the snow layers are the primary driver of convection in our models.

[23] The thickness of the snow layer is another quantity which can vary widely depending on the sulfur content and on the adiabat [Chen *et al.*, 2008]. We have chosen a deep snow layer thickness of $0.13r_o$. This falls within the range of values predicted from the data of Chen *et al.* [2008]. Investigating the effect of snow layer thickness on the dynamo will be the goal of future work in this field. In this study, the deep snow zone extends from $0.61R_{CMB}$ to $0.74R_{CMB}$, where R_{CMB} is assumed to be $0.75R_M$.

[24] The nondimensional parameters in equations (2)–(5) are the Rayleigh number (Ra), the magnetic Rossby number (Ro), the magnetic Prandtl number (q_κ), and the Ekman number (E). These are given by

$$Ra = \frac{\alpha_T g_o h_c r_o^2}{2\Omega\eta} \quad (9)$$

$$Ro = \frac{\eta}{2\Omega r_o^2} \quad (10)$$

$$q_\kappa = \frac{\kappa}{\eta} \quad (11)$$

$$E = \frac{\nu}{2\Omega r_o^2} \quad (12)$$

where α_T is the codensity expansion coefficient, g_o is the gravitational acceleration at the core mantle boundary, ν is the kinematic viscosity, and κ is the codensity diffusivity.

[25] In all cases the maximum spherical harmonic degree is 33 and the maximum order is 21. In the radial direction

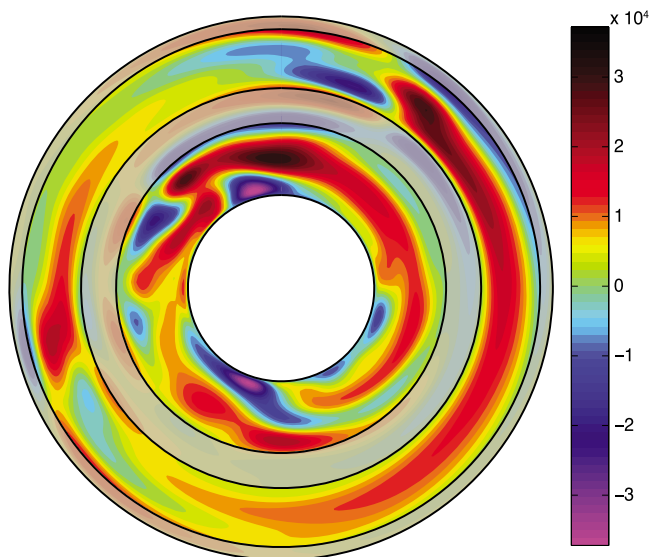


Figure 2. A snapshot of axial vorticity in the equatorial plane for a double snow state model (model 1). Here, the snow layers have been shaded gray. The units are nondimensional.

we used 119 grid points, 36 of which were in the inner core, 64 of which were in the fluid region and 19 of which were in the thin, weakly conducting mantle layer. In the fluid region, the grid points for the codensity and magnetic fields were positioned at the extrema of the Chebyshev polynomial T_{64} in order to provide maximum resolution in the boundary

regions. The fluid flow is solved spectrally using an expansion in Chebyshev polynomials.

[26] Our models use hyperdiffusivities with the magnetic field, velocity field and codensity perturbation in order to work at more strongly supercritical Rayleigh numbers than would otherwise be possible. Our viscous, codensity and magnetic diffusivities vary with spherical harmonic degree l (for $l \geq l_o$) as

$$\eta(l) = \eta_0 (1 + 0.06(l - l_o)^2) \quad (13)$$

$$\kappa(l) = \kappa_0 (1 + 0.06(l - l_o)^2) \quad (14)$$

$$\nu(l) = \nu_0 (1 + 0.05(l - l_o)^2) \quad (15)$$

where η_0 , ν_0 and κ_0 are the diffusivities in the nondimensional parameters. For degrees less than l_o ($l < l_o$) no hyperdiffusivities are applied. The models presented here have $l_o = 0$ except when otherwise stated. For a review of the possible dynamical effects of hyperdiffusivities see *Zhang et al.* [1998] and *Grote et al.* [2000], but note that the diffusivities employed in these references go as l^3 (compared to l^2 in this study) and have larger prefactors than the ones used here. The hyperdiffusivities used in those studies are much more severe than the ones we use, so the conclusions they reach may not be applicable here. In all our models, we have ensured proper numerical convergence by requiring that the energies in the lowest degrees are several orders of magnitude larger than the energies in the higher degrees. Prelimi-

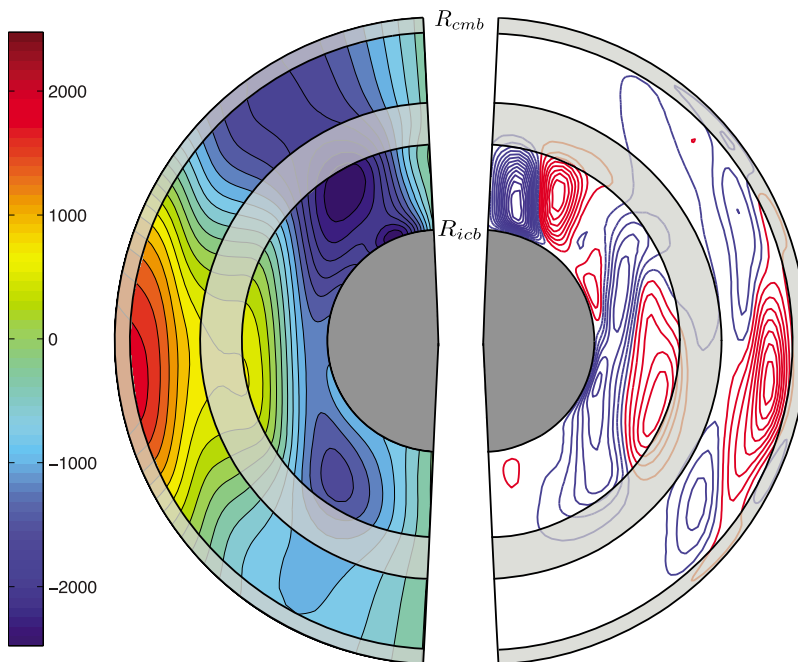


Figure 3. (left) Contours of the axisymmetric toroidal component of the velocity and (right) streamlines of the axisymmetric poloidal velocity for a double snow state model, averaged over 0.35 dipole magnetic diffusion times. In Figure 3 (right) the color denotes the direction of the flow: red is clockwise and blue is counterclockwise. Here, the snow layers have been shaded gray. The units are nondimensional.

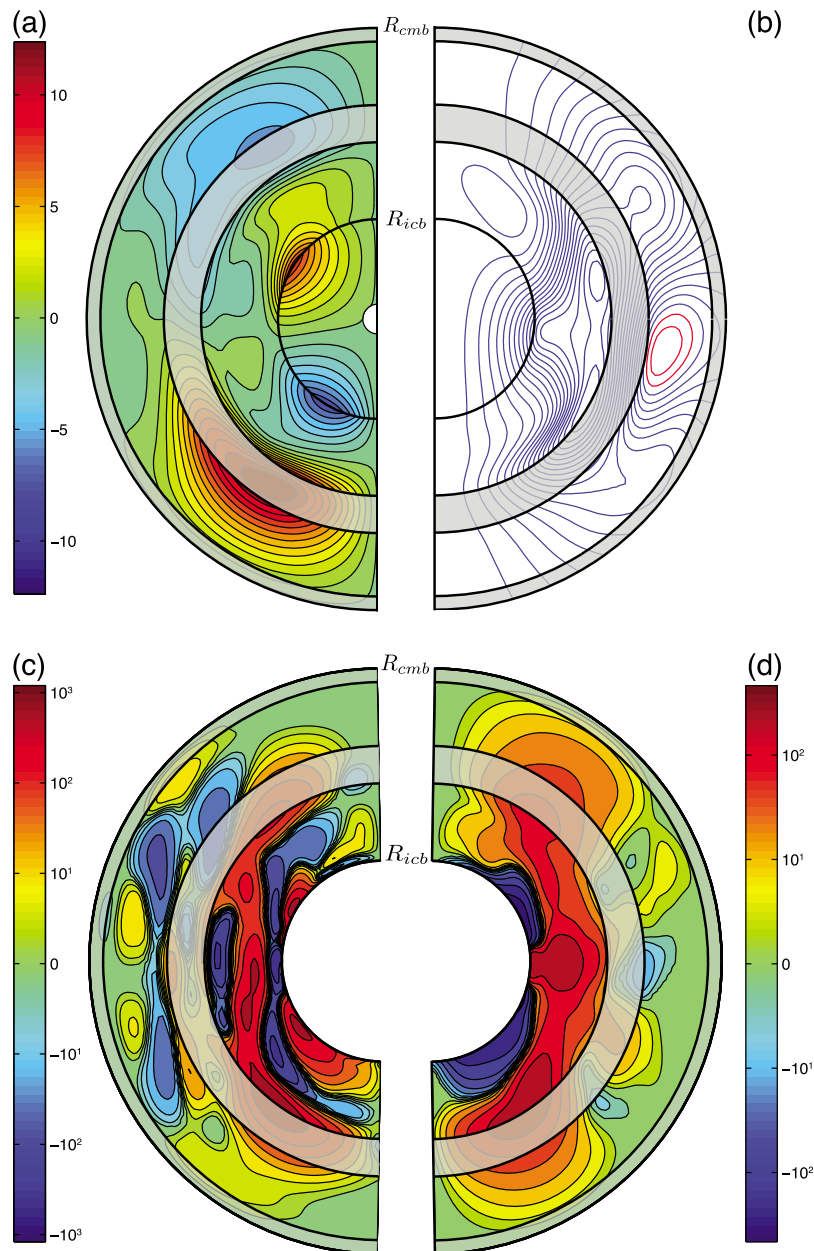


Figure 4. (a) Contours of the axisymmetric component of the toroidal field for a double snow state model. (b) Streamlines of the axisymmetric poloidal field for a double snow state model. The color of the streamline denotes the direction of the field: red is clockwise and blue is counterclockwise. (c) An axisymmetric slice of the generation of toroidal magnetic field energy due to stretching of poloidal magnetic field ($\mathbf{B}_T \cdot [(\mathbf{B}_p \cdot \nabla) \mathbf{u}]$) for a double snow state model. (d) An axisymmetric slice of the generation of poloidal magnetic field energy due to stretching of toroidal magnetic field ($\mathbf{B}_p \cdot [(\mathbf{B}_T \cdot \nabla) \mathbf{u}]$) for a double snow state model. Figures 4a–4d are from model 1 and have been averaged over the same period as Figure 3. The snow layers have been shaded gray. The units are nondimensional.

nary results on higher-resolution runs ($L_{\max} = 90$, $m_{\max} = 85$, $n_r = 95$) show that the resolution we run our models at is not an issue when hyperdiffusivities are used ($l_o = 0$).

[27] In all models presented here, constant codensity flux boundary conditions were applied to both the inner core boundary and the core mantle boundary. When constant codensity boundary conditions were used instead, there was no significant qualitative differences in the models. We

expect that the addition of snow layers to the core of Mercury would result in sources of buoyancy in addition to the typical buoyancy sources in the core (secular cooling, latent heat of solidification, and compositional buoyancy).

[28] In all cases we kept the inner core to outer core radius ratio (r_{io}) fixed at 12/35. This is consistent with the predictions of *Hauck et al.* [2004] when they used sulfur contents high enough to develop double and deep snow

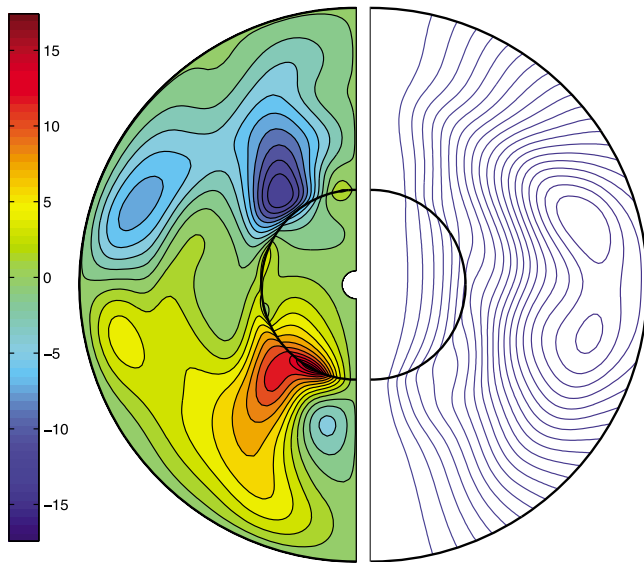


Figure 5. (left) Contours of the axisymmetric component of the toroidal field and (right) streamlines of the axisymmetric poloidal field for a snapshot of a strong field, Earth-like model (i.e., a model with no snow zones). The units are nondimensional.

states. In our study we chose a moderately low Ekman number of 2×10^{-5} to reduce the effects of viscosity in our model. Although this is much larger than the Ekman number expected for Mercury (on the order of 10^{-13}), at present it is numerically infeasible to work at such low Ekman numbers. Stress free boundary conditions are also used to minimize Ekman boundary layer effects, which would be far too large if we chose to use no-slip boundary conditions. We used finite electrically conducting boundary conditions on the magnetic field. We also set our magnetic Rossby number to be 2×10^{-5} , and set both of our Prandtl numbers to 1. Only the modified Rayleigh number and initial conditions were varied between the models. In these models the critical Rayleigh number is approximately 700.

3. Results

3.1. Dipole Moment

[29] *Chen et al.* [2008] outline three basic configurations for iron snow zones in Mercury's core: a single snow zone at the CMB (shallow snow state), a snow zone at the CMB along with one midway through the core (double snow state), and a single snow zone midway through the core (deep snow state). We found that only models with a deep snow layer (double and deep snow states) which does not

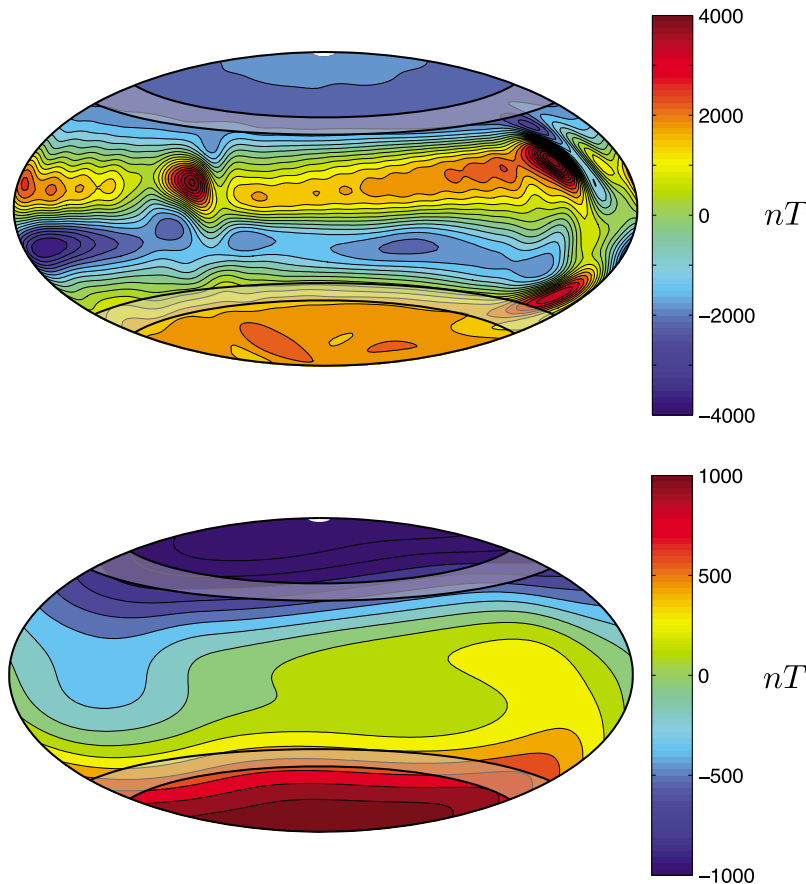


Figure 6. The radial magnetic field for model 1 (top) at the CMB and (bottom) at the surface at the same instant in time as Figure 2. The tangent cylinder formed by the deep snow layer has been shaded gray.

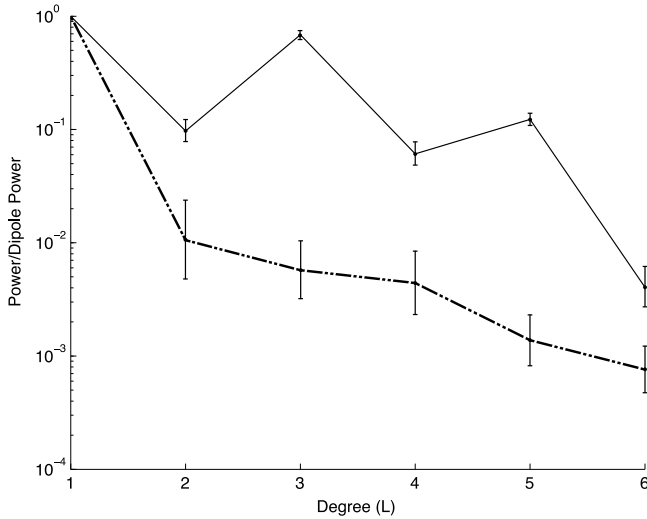


Figure 7. Temporally averaged surface power spectra for an Earth-like model (i.e., a model without snow zones) (dashed) and for a double snow state model (solid, model 1) averaged over the same time period as Figure 3 at the surface of a Mercury-like planet ($R_{\text{cmb}} = 0.75$). Both models have been averaged over 0.35 dipole magnetic diffusion times. The error bars on the power spectrum for the model indicate one standard deviation of the power over the averaging window.

extend to the ICB successfully produced a weak dipolar field. The results for the simulations of interest are summarized in Table 1. In all cases the dipole moment was relatively stable. Although several dipole reversals did occur, the field usually returned to a stable configuration akin to its prereversal state, though of opposite polarity. In most models the dipole tilt is quite small, for a nonreversing segment of model 2, the dipole tilt averaged over approximately half a magnetic diffusion time was 6° away from the rotation axis.

3.2. Velocity Fields

[30] The most immediate effect of the deep snow layer is to isolate the regions above and below the layer, there is very little fluid flowing across the snow layer. Convection columns form in both convecting regions, and do not appear to have any spatial or temporal correlation. In Figure 2 the axial vorticity in the equatorial plane is plotted. The regions of solid color correspond to convection columns aligned with the rotation axis and the sign of the vorticity indicates the direction the column is rotating. The convection columns are coaxial with the rotation axis and do not cut across the stably stratified layer. Although there are patches of vorticity inside the stable layer, these are all due to viscous coupling to an opposite patch of vorticity in the convective region and do not contribute to dynamo generation processes.

[31] The snow layer also has consequences for the axisymmetric flows. In Figure 3 the axisymmetric toroidal (left) and poloidal (right) components of velocity are plotted. Examining the toroidal component of velocity, we see that the snow zones, especially the deep snow zone, bend the zonal flow contours significantly. The regions closest to

the rotation axis are dominated by a retrograde flow, while the regions in the equatorial region near the CMB have an overall prograde flow. Examining the poloidal velocity field (Figure 3, right) we see that most of the poloidal flow occurs in the inner dynamo region. In the outer region, convection is concentrated in the equatorial region with little convection occurring inside the tangent cylinder formed by the deep snow layer.

3.3. Magnetic Field

[32] The nature of this dynamo is revealed if we examine the generation mechanisms for both toroidal and poloidal fields. Figure 4a shows the axisymmetric toroidal field for a double snow state model. When compared to an Earth-like model (i.e., no snow zones) (Figure 5, left), it appears as though there are two dynamos of opposite polarity operating within the same core of the double snow state model. Further evidence for this “double dynamo” interpretation is found by examining the radial magnetic field at the CMB (Figure 6, top). In Figure 6 the intersection of the tangent cylinder formed by the deep snow zone with the CMB is shaded gray. We note that there seem to be no features in the radial magnetic field at the CMB from the tangent cylinder of the inner core [Stanley *et al.*, 2007], while the deep snow zone’s tangent cylinder serves as the border between radial field of opposing sign. Also, the prominent flux spots in the equatorial region do not occur poleward of the tangent cylinder formed by the deep snow layer.

[33] In Figure 6 (top), which plots the radial component of the magnetic field at the CMB for model 1, a strong octupolar signature is seen (Figure 7 and Table 1). The magnetic field generated by the dynamo region nearest to the inner core is expressed in the polar regions, while the equatorial regions are dominated by the field generated in the outer dynamo region. If we observe the radial magnetic field for different radii inside the core, the inverted polarity in the equatorial region does not appear until outside the deep snow zone, indicating a source in the outer dynamo region.

3.4. Dynamo Mechanism

3.4.1. Generation of the Toroidal Field

[34] The inverted polarity of the toroidal magnetic field in the outer region can be understood by examining the dominant ω effect component of the toroidal field generation in our models. From equation (4), the growth of axisymmetric energy in the toroidal magnetic field can be written as

$$\mathbf{B}_T \cdot \frac{\partial \mathbf{B}_T}{\partial t} = \mathbf{B}_T \cdot [(\mathbf{B} \cdot \nabla) \mathbf{u}] - \mathbf{B}_T \cdot [(\mathbf{u} \cdot \nabla) \mathbf{B}] \quad (16)$$

The first term on the right describes the growth of energy in the toroidal field due to stretching of magnetic field lines while the second describes the growth of toroidal field energy due to the advection of toroidal field. Focussing on the stretching term, the direction of the resultant toroidal field is dependent on the direction of the initial field and on the sign of the gradient of velocity which is shearing it. Figure 3 (left) shows the axisymmetric toroidal component of the flow. Here, the stably stratified layer causes differential rotation in the z direction. Examining the midlatitude regions where the flow is

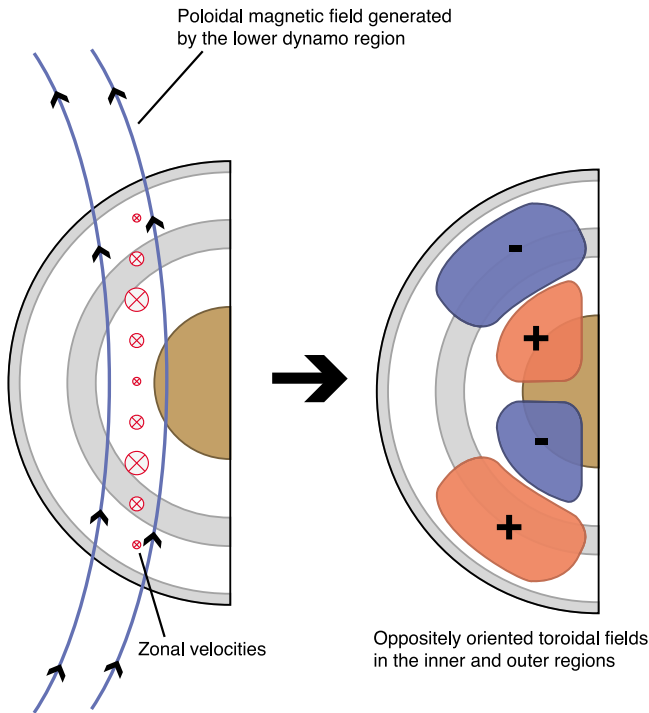


Figure 8. A schematic diagram of the generation of the toroidal field in a double snow state model. On the left, red arrowheads (going into the page) represent zonal velocities whose strength is proportional to the arrow head size. Moving in the direction of the poloidal field line, an increase in zonal velocity (i.e., a positive gradient) results in positively signed toroidal field generation. Conversely, a decrease in zonal velocity (i.e., a negative gradient) results in negatively signed toroidal field generation. These act on poloidal magnetic fields (blue) to create the characteristic toroidal field we observed in our models. The snow layers have been shaded gray.

strongest, we see that the gradient in \mathbf{u} changes sign just below the stable layer. An initially poloidal magnetic field which originates from the inner dynamo will be sheared by this differential rotation. The shear in the outer region will generate toroidal field which is opposite in sign to the toroidal field in the inner region. This process can be seen in Figure 4c, which plots the axisymmetric growth of toroidal field energy caused by the stretching of poloidal magnetic field lines ($\mathbf{B}_T \cdot (\mathbf{B}_p \cdot \nabla) \mathbf{u}$). We see that significant amounts of poloidal field are converted into toroidal field in the midlatitudes of the outer region and deep snow layer, effectively seeding the outer region with toroidal field. Although there are other ways that toroidal field can be generated in the outer region (for example by stretching toroidal field) this is the dominant method in our models. Figure 8 shows a schematic diagram of this process.

3.4.2. Generation of the Poloidal Field

[35] Poloidal fields in both the inner and outer regions are generated by convective motions acting on toroidal fields. In the inner region, convection is stronger and a strong dipolar field is generated. However, the dipole field observed outside the core is weak due to a combination of three processes, which all stem from the presence of a deep snow

layer. A schematic diagram illustrating these three processes is shown in Figure 9.

[36] First, the inner dynamo region does most of the field generation, but since it is removed from the CMB (due to the presence of the outer layer), its strength is reduced. This is similar to the mechanism behind the weak magnetic field observed by *Christensen* [2006], however, this is not the sole reason for the overall weakness of the field in our models. In the work of *Christensen* [2006] the parameters were chosen such that magnetic field at the top of the dynamo generation region was both strong and nondipolar. Although placing the dynamo generation away from the surface does weaken the dipole moment observed at the surface, the primary reason their model possesses a weak dipole moment is because most of the power lies in higher multipoles which vary quickly in time and are preferentially attenuated due to the skin effect. To determine whether our fields are weak solely due to the skin effect, we ran a deep snow state model, in which the region above the lower boundary of the deep snow zone was strongly stably stratified. This ensured that no dynamo action would occur in the outer region, and that any weakening of the field observed would be solely due to the skin effect or the removal of the dynamo region from the surface. We found that when we did this, the magnetic field was stronger than in our models containing a convective upper region by approximately an order of magnitude. From this analysis we conclude that flows in the outer region play an important role in the attenuation of the overall field in our models.

[37] Secondly, additional weakening of the dipole moment in our models occurs through the theft of flux by meridional flows in the outer dynamo region. The density of

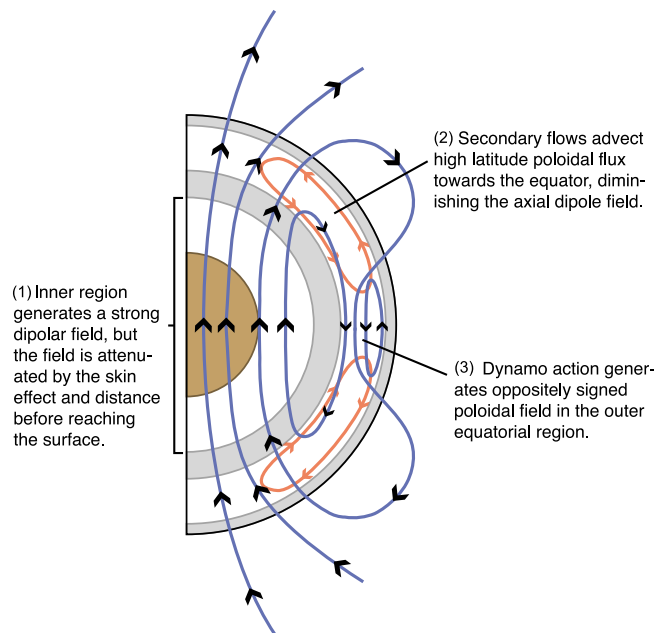


Figure 9. A schematic diagram of the generation of the poloidal magnetic field in a double snow state model. Blue lines represent poloidal magnetic field lines, and red lines represent meridional flows. The three mechanisms discussed in the text for weakening the observed field are marked (1), (2), and (3). The snow layers have been shaded gray.

poloidal magnetic field lines is reduced in the midlatitudes of the outer region in Figure 4b, as the field lines are advected toward the equator by meridional flows in this region (see Figure 9 for a schematic representation of this).

[38] Finally, dynamo action in the outer region weakens the observed surface field. The conversion of the toroidal field in the midlatitudes of the outer region into poloidal field can be seen when we plot the axisymmetric growth of poloidal field energy caused by the stretching of toroidal magnetic fields ($\mathbf{B}_T \cdot (\mathbf{B}_p \cdot \nabla) \mathbf{u}$) which is plotted in Figure 4d. When this is compared with the axisymmetric streamlines of poloidal magnetic field in Figure 4b we see that the source of the equatorial poloidal field we observe is the midlatitude toroidal flux sheared out by the snow layer. Since the outer dynamo region is seeded with toroidal field which is opposite in polarity to that of the inner dynamo region, convection will generate a poloidal field in the outer region of opposite sign to the field generated by the inner region. Evidence that the outer dynamo region would operate in this way comes from studies of dynamos in thin shells (similar to the geometry of the outer shell) which show that at similar Rayleigh numbers to the ones used here, dipolar fields result [Stanley *et al.*, 2005]. In the outer region we observe a very similar field morphology as Stanley *et al.* [2005], implying that if both regions generated poloidal field independently, the resulting fields would be of opposite polarity. Since they occur within the same core, they superpose and contribute to the weak observed surface field.

[39] The polarity of the outer dynamo is entirely determined by the inner dynamo. Since the outer region is being primed with a toroidal field by the inner region, and since convection is relatively weak in the outer region, it is unlikely that this dynamo could ever determine its polarity independent of the inner region. The situation of a dynamo being immersed in an externally applied field was examined by Sarson *et al.* [1997]. In that case a dynamo was immersed in a constant background field, giving the dynamo an external source of poloidal field, which it could then convert to toroidal field. In our case the opposite occurs, the inner dynamo region supplies the outer dynamo region with a toroidal field which this region then converts to poloidal field.

[40] When a double snow state model reverses, it is the inner dynamo that leads the reversal. During the reversal, the dipole moment decays to only a few nT- R_M^3 . After the reversal finishes, the same differential rotation in z occurs, so the outer dynamo region once again becomes active with the opposite sign as the inner dynamo region.

[41] In our models we chose parameters such that the magnetic Reynolds numbers of our snow zone models are comparable to the Earth-like dynamo model in Figure 5. We define our magnetic Reynolds number as

$$\text{Re}_M = \frac{1}{V} \int_V \frac{|\nabla \times (\mathbf{u} \times \mathbf{B})|}{|\nabla^2 \mathbf{B}|} \quad (17)$$

We have done this to ensure that any change in field strength we observe is not the result of a different efficiency of magnetic field generation. The difference in the field intensity at the surface can therefore be attributed to the change in field morphology resulting from the snow zones.

Other studies [Christensen and Aubert, 2006] have shown that Earth-like dynamo models have a critical magnetic Reynolds number of order 50. The Earth-like dynamo model in Figure 5 and our double snow state models have magnetic Reynolds numbers in the range of 48–62.

4. Discussion

[42] We have shown that introducing exotic (yet predicted) sources of compositional driving can produce a dipole moment as weak as the measured moment of Mercury. Although both the deep and double snow states produced dipole moments weaker than one would expect from scaling arguments, the double snow states most closely match the observations of Mercury. The deep snow state is also less likely than the double snow state due to the high (> 10% wt) sulfur content it requires [Rivoldini *et al.*, 2009].

[43] Owing to the reduction in length scale caused by the addition of the stably stratified layer, our models in a double or deep snow state geometry must operate at Rayleigh numbers which are more than 40 times supercritical in order to sustain a magnetic field against ohmic decay. For example, although they use a slightly different geometry and different boundary conditions, Christensen [2006] shows that $\text{Ra} > 50\text{Ra}_c$ for dynamo onset in the parameter regime of our snow zone models (in order to make this comparison, one must convert our definition of the Ekman number to one in terms of shell thickness rather than core radius, using the thickness of the lower dynamo region as the shell thickness). Our double snow state models operate with a Christensen and Aubert defined Ekman number ($E_{ca} = \nu / \Omega D^2$) of approximately 5×10^{-4} . Since we must operate at highly supercritical Rayleigh numbers, we must turn to hyperdiffusivities for computational reasons. We have run high-resolution runs ($L_{\text{max}} = 90$, $m_{\text{max}} = 85$, $n_r = 65$) at lower (7.9Ra_c) supercritical Rayleigh numbers with minimal ($l_o = 40$, in equations (13)–(15)) or absent hyperdiffusivities, however these supercriticalities are too low to sustain magnetic fields. The absence of dynamo action at these low Rayleigh numbers when hyperdiffusivities are not used implies that small-scale fluid motions, which are preferentially damped in our models that use hyperdiffusivities, are not responsible for the large-scale field generation.

[44] The mechanisms behind the formation of the dynamo state we observe are expected to be robust to hyperdiffusivities. Fluid motions in the lower dynamo region should produce a dipolar seed field irrespective of whether hyperdiffusivities are present. The principle reason for the pattern of toroidal fields we observe in our study is differential rotation in the radial direction at midlatitudes. Finally, the transport of flux toward the equator is caused by large-scale secondary flows which occur in dynamos without hyperdiffusivities as well.

[45] This system is likely to evolve in time substantially. Over long time scales the upper dynamo region should become preferentially enriched in sulfur and the lower region should become preferentially enriched in iron and eventually stratified down to the ICB as the zone of potential snow formation grows with cooling. Furthermore, the region nearest the CMB could form a stratified layer of light element similar to the kind proposed for the Earth [Braginsky, 2006]. This stratified ocean would coexist with the stratified

region which we have already placed near the CMB. All these effects vary on time scales much longer than those associated with the dynamo, so they have been neglected here. Future work will focus on understanding the long-term thermal and compositional evolution of a double snow state system. However, should future observations of Mercury's magnetic field confirm field characteristics consistent with the double snow zone model, this would place important constraints on the present-day structure of the planet's core.

[46] In this study we have only examined situations that result in the outer dynamo region generating little field on its own. Understanding the consequences of increasing the Rayleigh number, which should lead to an increase the vigor of convection in the outer dynamo region will be an area of interesting future research.

[47] The magnetic field produced by a geometry containing a deep snow layer is quite distinct. For the r_{io} value used in this study (0.34), the octupole component is always much larger than the quadrupole component and is comparable to the dipole component. Future work will determine the dependence of the spectra on different inner core sizes as it could potentially be a useful clue for the MESSENGER and BepiColombo missions to Mercury.

[48] **Acknowledgments.** We thank the Associate Editor and two anonymous reviewers for helpful comments that greatly improved this manuscript. This work was partially funded by the National Science and Engineering Research Council of Canada (NSERC) and the Ontario Early Researcher Award Program. Computations were performed on supercomputing resources partially funded by the Canadian Foundation for Innovation and the Ontario Research Fund, and on the gpc and tes supercomputers at the SciNet HPC Consortium. SciNet is funded by the Canada Foundation for Innovation under the auspices of Compute Canada, the Government of Ontario, Ontario Research Fund—Research Excellence, and the University of Toronto. Partial support was also provided by NASA's MESSENGER Participating Scientist program (NNX07AR77G).

References

- Aharonson, O., M. T. Zuber, and S. C. Solomon (2004), Crustal remanence in an internally magnetized non-uniform shell: a possible source for Mercury's magnetic field?, *Earth Planet. Sci. Lett.*, 261–268, doi:10.1016/S0012-821X(03)00682-4.
- Anderson, B. J., et al. (2009), The magnetic field of Mercury, *Space Sci. Rev.*, 152, 307–339.
- Braginsky, S. I. (2006), Formation of the stratified ocean of the core, *Earth Planet. Sci. Lett.*, 650–656, doi:10.1016/j.epsl.2006.01.029.
- Braginsky, S. I., and P. H. Roberts (1995), Equations governing convection in Earth's core and the geodynamo, *Geophys. Astrophys. Fluid Dyn.*, 1–97.
- Breuer, D., S. A. Hauck II, M. Buske, M. Pauer, and T. Spohn (2007), Interior evolution of Mercury, *Space Sci. Rev.*, 229–260.
- Chen, B., J. Li, and S. A. Hauck II (2008), Non-ideal liquidus curve in the Fe-S system and Mercury's snowing core, *Geophys. Res. Lett.*, L07201, doi:10.1029/2008GL033311.
- Christensen, U. R. (2006), A deep dynamo generating Mercury's magnetic field, *Nature*, 1056–1058, doi:10.1038/nature05342.
- Christensen, U. R., and J. Aubert (2006), Scaling properties of convection-driven dynamos in rotating spherical shells and application to planetary magnetic fields, *Geophys. J. Int.*, 97–114, doi:10.1111/j.1365-246X.2006.03009.x.
- Christensen, U. R., and J. Wicht (2007), Numerical dynamo simulations, in *Treatise on Geophysics*, vol. 8, edited by P. Olson, pp. 245–282, Elsevier, Amsterdam.
- Conzelmann, V., and T. Spohn (1999), New thermal evolution models suggesting a hot, partially molten Mercurian interior, *Bull. Am. Astron. Soc.*, 1102.
- Glassmeier, K. H., H. U. Auster, and U. Motschmann (2007), A feedback dynamo generating Mercury's magnetic field, *Geophys. Res. Lett.*, L22201, doi:10.1029/2007GL031662.
- Glatzmaier, G. A. (2002), Geodynamo simulations: How realistic are they?, *Annu. Rev. Earth Planet. Sci.*, 237–257, doi:10.1146/annurev.earth.30.091201.140817.
- Grote, E., F. H. Busse, and A. Tilgner (2000), Effects of hyperdiffusivities on dynamo simulations, *Geophys. Res. Lett.*, 27, 2001–2004.
- Hauck, S. A., II, A. J. Dombard, R. J. Phillips, and S. C. Solomon (2004), Internal and tectonic evolution of Mercury, *Earth Planet. Sci. Lett.*, 222, 713–728.
- Hauck, S. A., II, J. M. Aurnou, and A. J. Dombard (2006), Sulfur's impact on core evolution and magnetic field generation on Ganymede, *J. Geophys. Res.*, 111, E09008, doi:10.1029/2005JE002557.
- Heimpel, M. H., J. M. Aurnou, F. M. Al-Shamali, and N. Gómez Pérez (2005), A numerical study of dynamo action as a function of spherical shell geometry, *Earth Planet. Sci. Lett.*, 542–557, doi:10.1016/j.epsl.2005.04.032.
- Heyner, D., D. Schmitt, J. Wicht, K. H. Glassmeier, H. Korth, and U. Motschmann (2010), The initial temporal evolution of a feedback dynamo for Mercury, *Geophys. Astrophys. Fluid Dyn.*, 104, 419–429.
- Kuang, W., and J. Bloxham (1997), An Earth-like numerical dynamo model, *Nature*, 371–374.
- Kuang, W., and J. Bloxham (1999), Numerical modeling of magnetohydrodynamic convection in a rapidly rotating spherical shell: Weak and strong field dynamo action, *J. Comput. Phys.*, 51–81.
- Levy, E. H. (1979), Planetary dynamo amplification of ambient magnetic fields, *Proc. Lunar Planet. Sci. Conf.*, 10th, 2335–2342.
- Ness, N. F., K. W. Behannon, R. P. Lepping, and Y. C. Whang (1976), Observations of Mercury's magnetic field, *Icarus*, 479–488.
- Margot, J. L., S. J. Peale, R. F. Jurgens, M. A. Slade, and I. V. Holin (2007), Large longitude libration of Mercury reveals a molten core, *Science*, 710–714, doi:10.1126/science.1140514.
- Olson, P., and U. Christensen (2006), Dipole moment scaling for convection-driven planetary dynamos, *Earth Planet. Sci. Lett.*, 561–571, doi:10.1016/j.epsl.2006.08.008.
- Purucker, M. E., C. L. Johnson, B. J. Anderson, H. Korth, H. Uno, D. T. Blewett, T. J. Sabaka, S. C. Solomon, and J. W. Head (2009), Mercury's internal magnetic field from MESSENGER, *Lunar Planet. Sci.*, XL, Abstract 1277.
- Rivoldini, A., T. Van Hoolst, and O. Verhoeven (2009), The interior structure of Mercury and its core sulfur content, *Icarus*, 12–30, doi:10.1016/j.icarus.2008.12.020.
- Sarson, G. R., C. A. Jones, K. Zhang, and G. Schubert (1997), Magnetohydrodynamic dynamos and the magnetic fields of Io and Ganymede, *Science*, 1106–1108.
- Schubert, G., M. N. Ross, D. J. Stevenson, and T. Spohn (1988), Mercury's thermal history and the generation of its magnetic field, in *Mercury*, edited by F. Vilas et al., pp. 429–460, Univ. of Ariz. Press, Tucson.
- Stanley, S., and J. Bloxham (2006), Numerical dynamo models of Uranus and Neptune's magnetic fields, *Icarus*, 556–572.
- Stanley, S., and A. Mohammadi (2008), Effects of an outer thin stably stratified layer on planetary dynamos, *Phys. Earth Planet. Int.*, 179–190, doi:10.1016/j.pepi.2008.06.016.
- Stanley, S., J. Bloxham, W. E. Hutchison, and M. T. Zuber (2005), Thin shell dynamo models consistent with Mercury's weak observed magnetic field, *Earth Planet. Sci. Lett.*, 27–38, doi:10.1016/j.epsl.2005.02.040.
- Stanley, S., M. T. Zuber, and J. Bloxham (2007), Using reversed magnetic flux spots to determine a planet's inner core size, *Geophys. Res. Lett.*, L19205, doi:10.1029/2007GL030892.
- Stevenson, D. J. (1987), Mercury's magnetic field: A thermoelectric dynamo?, *Earth Planet. Sci. Lett.*, 114–120.
- Stewart, A. J., M. W. Schmidt, W. van Westrenen, and C. Lieske (2007), Mars: A new core-crystallization regime, *Science*, 316, 1323–1325.
- Takahashi, F., and M. Matsushima (2006), Dipolar and non-dipolar dynamos in a thin shell geometry with implications for the magnetic field of Mercury, *Geophys. Res. Lett.*, L10202, doi:10.1029/2006GL025792.
- Uno, H., C. L. Johnson, B. J. Anderson, H. Korth, and S. C. Solomon (2009), Modeling Mercury's internal magnetic field with smooth inversions, *Earth Planet. Sci. Lett.*, 328–339, doi:10.1016/j.epsl.2009.02.032.
- Wicht, J., M. Mandea, F. Takahashi, U. R. Christensen, M. Matsushima, and B. Langlais (2007), The origin of Mercury's internal magnetic field, *Space Sci. Rev.*, 132, 261–290, doi:10.1007/s11214-007-9280-5.
- Zhang, K., C. Jones, and G. Sarson (1998), The dynamical effects of hyperviscosity on numerical geodynamo models, *Stud. Geophys. Geod.*, 42, 247–253.

S. A. Hauck II, Department of Geological Sciences, Case Western Reserve University, Cleveland, OH 44106, USA.

S. Stanley and R. Vilim, Department of Physics, University of Toronto, 60 St. George St., Toronto, ON M5S 1A7, Canada. (rvilim@physics.utoronto.ca)